4

Near-surface reflection surveying

J.-L. Mari

Seismic reflection is the most widely used seismic technique. It has the advantage of being able to provide a picture of the subsurface in two or three dimensions (2D or 3D) in a regular grid (Figure 4.1).

For the last two decades there has been significant progress in 3D seismic technology. Between 1990 and 1996 there was an exponential increase in the number of 3D seismic surveys carried out by many major oil companies to cover their offshore fields. Today, 3D land seismic acquisition is also developing very rapidly. The technology has reduced many uncertainties in oil and gas exploration and production, and it benefits greatly from developments in other fields such as computing, GPS positioning, an increased number of channels in instrument recording, improvements in processing software, etc. 3D data are now increasingly used for field development and production and not only as an exploration tool. Pre-planning of

DOI: 10.1051/978-2-7598-2351-2.c006

3D surveys has become a fundamental step to ensure that the 3D data quality meets structural, stratigraphical and lithological requirements. Pre-planning includes the evaluation of both geophysical and non-geophysical parameters such as environmental considerations, health and safety requirements, etc. Specific pre-planning tools (Cordsen A., Galbraith M., Peirce J., 2000) have been developed to estimate all acquisition characteristics such as offset, fold and azimuth distributions, effects of surface obstacles, etc. Pre-planning steps aim to define the geological targets of the 3D survey, with the associated geophysical parameters, design and costs.

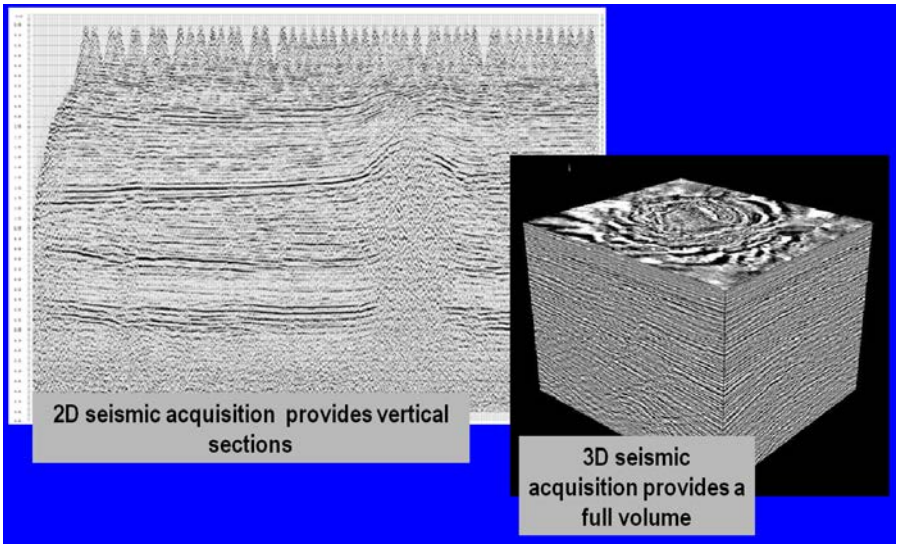

Figure 4.1 *2D and 3D seismic imaging (after J. Meunier, 2004, IFP School course).*

In 2D acquisition, the image obtained after processing is a vertical seismic section. The horizontal axis of the section represents the geographical abscissa of subsurface points along the acquisition profile, and the vertical axis represents the record time. The seismic events that appear on the records correspond to the arrivals of waves reflected at normal incidence on the seismic horizons. The seismic horizons correspond to discontinuities of acoustic impedance; their picks provide a structural image of the subsurface.

3D seismic acquisition provides full volume interpretation, consisting of a collection of sections parallel to each other. Surface seismic has vertical and horizontal resolutions measured in tens of meters with lateral investigation distances only limited by the size of the area investigated by the seismic surveys.

This chapter is neither a basic introduction nor a theoretical study of seismic acquisition and processing; its goal is to show, through the use of field examples, the contribution of seismic reflection to near-surface imaging, and to hydrogeological

studies. For each field example we have described the survey design (acquisition parameters) and the applied processing sequence.

The reader will find more information about acquisition and survey design in Galbraith (2000), Lansley (2000), Mayne (1962), Meunier and Gillot (2000), Meunier (2011), Monk and Yates (2000), Musser (2000), Vermeer and Hornman (2000), and Chaouch and Mari (2006); more about signal processing in Mari *et al.* (1999, 2015); and more on seismic processing in Yilmaz (1987), and Robein (2003).

4.1 General notes about acquisition and survey design

2D seismic acquisition is achieved with either end-on (also called off-end) or split dip spreads (Figure 4.2-a).

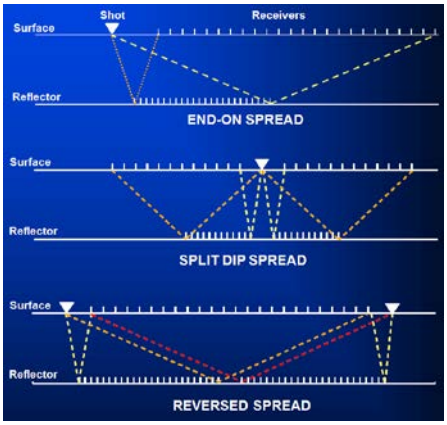

a

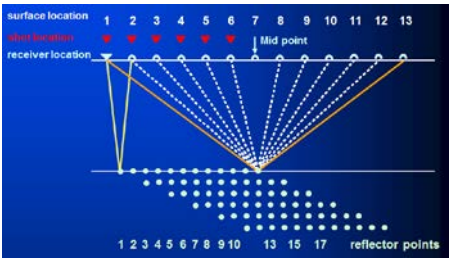

b

Figure 4.2 *2D land seismic acquisition: (a) seismic spreads, (b) stacking fold.*

The individual shot element is defined by the distance between the source and the first receiver, the number of receivers and the distance between two adjacent receivers. A receiver can be a single sensor (geophone for land acquisition) or an array of sensors. If the receiver is a single sensor, the interval between two receivers is of several meters, if it is an array, the interval is of several tens of meters. The maximum source-receiver offset to the far receiver is about the same as the maximum depth of the geological objective. The near receiver offset is chosen to minimize interference between ground roll (surface waves) and reflection arrivals. The distance between reflection points, assumed to be midpoints, is equal to half the receiver interval. For a receiver spread of length L, the length of the reflector illuminated is equal to half

the length of the spread (L/2). If the entire spread (source and receiver spreads) is shifted by L/2 then the reflection zone illuminated by the current shot adjoins that illuminated by the previous shot. Where there is no overlap between the successive reflection zones, the coverage is called single fold coverage.

If the distance between shots is m/2 times the receiver interval, where m is a submultiple of the number of receivers N, then there is an overlap between the reflection zones illuminated by successive shots; the reflection coverage is then termed multiple coverage, with the fold coverage being equal to N/m. Figure 4.2-b is an example of multiple coverage. A 12-receiver spread (N=12) is moved up by one receiver interval (m=2) to provide 6-fold coverage. The fold of coverage corresponds to the number of traces having the same common midpoint (CMP).

The distribution of offsets is regular in 2D surveys; the azimuth (angle between the theoretical direction of the seismic line and the straight line joining the source and the receiver) is constant (0° for end-on shooting, and 0° and 180° for split spread shooting).

Acquisition is more complex for 3D land surveys. Source and receiver lines are laid out to provide the most homogeneous coverage. The most conventional implementation is the cross-spread design with lines of sources perpendicular to lines of receivers (Figure 4.3).

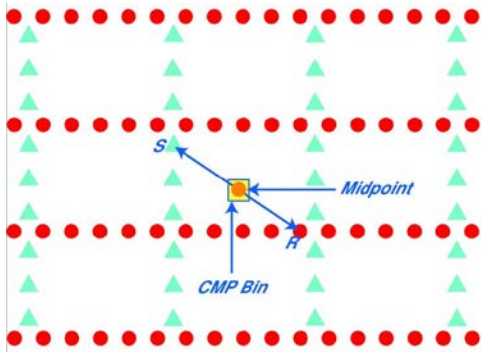

Figure 4.3 *Cross-spread design: Lines of sources (green triangles) perpendicular to lines of receivers (red dots).*

In 3D acquisition, the CMP is replaced by a cell or bin, the size of which being the product of half the source interval and half the receiver interval. Traces contributing to the same CMP bin have irregularly distributed azimuths and offsets. Implementation is optimized to ensure the most regular azimuth and offset distribution possible. Figure 4.4-a shows a single fold 3D subset, obtained with an elementary cross spread for which source positions belong to the same source line, and receiver positions belong to the same receiver line. The stacking fold is the number of overlapping elementary cross spreads (Figure 4.4-b).

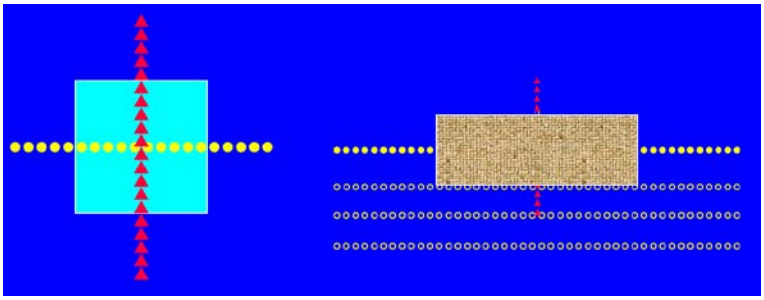

a

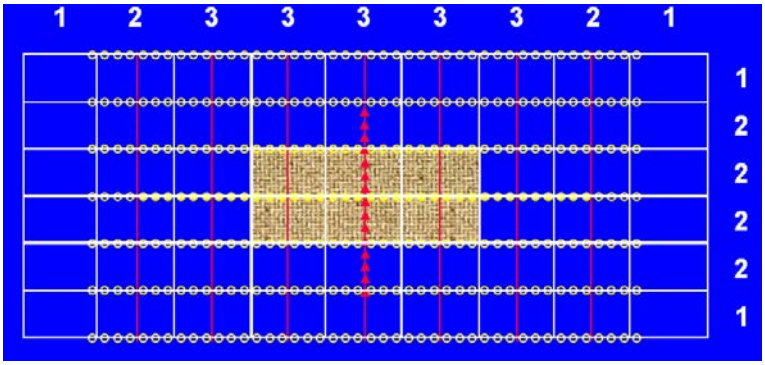

b

Figure 4.4 *3D land seismic acquisition (after J. Meunier, 2004, IFP School course). (a) Cross-spread build up: Cross-spread set of seismograms for which source positions belong to the same source line, and receiver positions belong to the same receiver line. (b) Stacking fold: number of overlapping cross-spreads (G. Vermeer).*

The data are correctly sampled if the geophone interval **i** is sufficiently small (several meters) to avoid spatial aliasing. In 3D acquisition, it is necessary to use telemetric recording systems to simultaneously record several thousands of traces (an elementary shot being composed of several lines of receivers and several hundred receivers per line). The undersampling in distance can be done by applying a wave number filter in processing. Another solution is to use field arrays of sensors and a specific acquisition design called stacked array geometry introduced by Anstey (1986).

For 2D surveys, a common midpoint can be viewed as a spatial filter, which is the convolution of a receiver array and a stack array. The geometry of acquisition must respect the following rules (Figure 4.5):

- Shot points (SP) should be recorded with a symmetric split dip spread,
- Source and receiver intervals should be the same,

- The SP should be located halfway between receivers,
- The receiver interval **e** should be **n** (number of sensors) times the sensor interval **i** (**e=ni**).

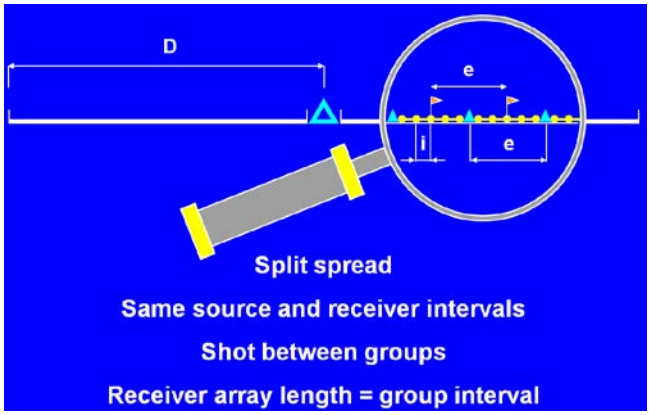

a

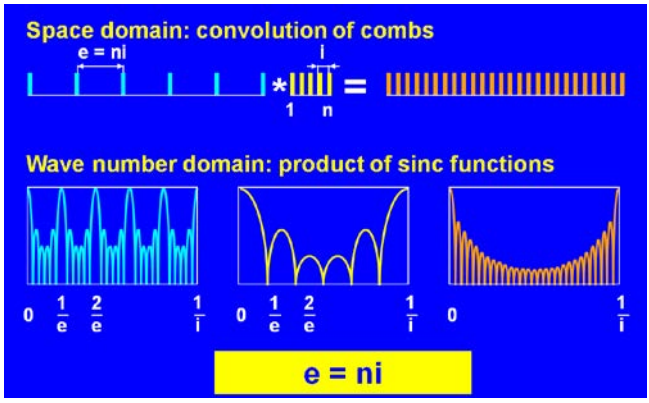

b

Figure 4.5 *2D stack array geometry (after J. Meunier, 2004, IFP School course); (a) 2D stack array rules; (b) convolution of 2 combs representing a receiver array and a stack array. Some wave numbers of the stack response are zeroed by notches of the receiver response, resulting in an unaliased combined response (from Meunier, 1998).*

The extension of the 2D stack array theory to 3D acquisition is not straightforward. Source and receiver lines become source and receiver grids (x, y) and 1D arrays (combs) become 2D arrays (brushes).

The geometry of acquisition (Figure 4.6) must respect the following rules (Meunier, 1999):

- Same source and same receiver interval **e** in x and y (full grid),
- Receiver–array size $\mathbf{n^2i^2}$ is equal to source and receiver intervals $\mathbf{e^2}$,
- Source and receiver grids are shifted by half an interval **e/2** in both directions.

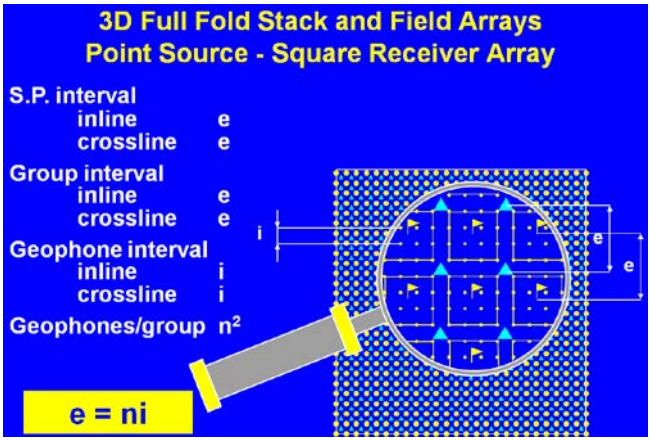

a

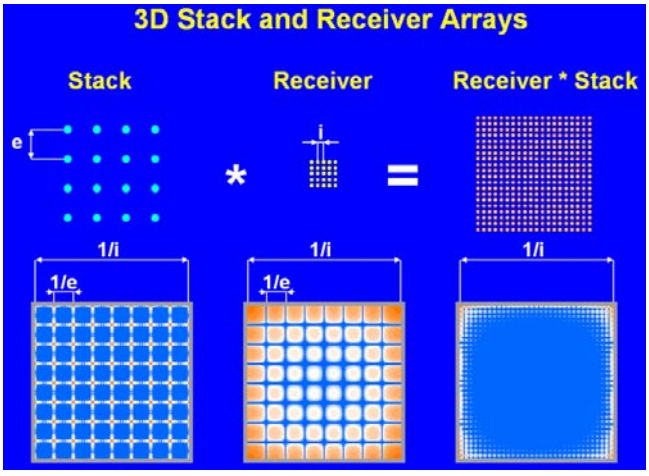

b

Figure 4.6 *3D stack array geometry (after J. Meunier, 2004, IFP School course). (a) 3D stack array rules; (b) convolution of the 3D receiver and stack arrays (Meunier, 1998).*

4.2 Comments on the reflection seismic processing sequence

The classical approach to seismic processing can be summarized in two main steps.

The first step includes pre-processing of the data and the application of static corrections. The purpose of pre-processing is to extract reflected waves from individual shots, by filtering out the parasitic events created by direct and refracted arrivals, surface waves, converted waves, multiples and noise. It is intended to compensate for amplitude losses related to propagation. Deconvolution operators are applied to improve resolution and harmonize records by taking into account source efficiency variations and eventual disparities between receivers. Any deconvolution is sensitive to noise. A classically used method that is relatively robust to noise is deconvolution with the Wiener filter. The Wiener filter allows the processing of a measured signal to obtain a desired signal. It minimizes (least squares conditions) the difference between the desired signal and the signal estimated by the filter. The desired signal can be a Dirac impulsion. In this case, spiking deconvolution is necessary. Static corrections, which are specific to land seismic surveys, are intended to compensate for weathered zone and topographic effects. Seismic records are sorted in common midpoint gathers or common offset gathers.

The second processing step is the conversion of common midpoint gathers or common offset gathers into time or depth migrated seismic sections. This second step includes the determination of the velocity model, with the use of stacking velocity analyses, or tomography methods. The role of migration is to place events in their proper location and increase lateral resolution, in particular by collapsing diffraction hyperbolas at their apex. Proper migration requires the definition of a coherent velocity field, which must be a field of actual geologic velocities in migrated positions. Determination of the velocity field is the most critical aspect of migration.

In near-surface experimentation, the separation of interfering wavefields is a crucial step to enhance reflected waves. To achieve this, wave separation filters such as F-K filters or SVD (Singular Value Decomposition) filters should be used.

4.3 Near-surface imaging

An experimental site at Vesdun (situated in the Cher region in central France) has been developed to train IFP School and university students, along with professionals. The geophysics training relates to the acquisition and processing of surface seismic data in 2D or 3D. A borehole has been drilled on site. It allows the acquisition of well seismic data such as vertical seismic profiles (VSP), and logging data such as full waveform acoustic data. The site is also used for experimental studies in near-surface geophysics.

Shot points recorded for near-surface seismic surveys are usually corrupted by surface waves such as pseudo-Rayleigh waves. For seismic imaging based on reflected waves, it is necessary to be able to separate weak reflected events from high energy surface waves. Wave separation is a crucial step in the processing sequence. We describe here the benefit of combining two different wave separation methods to remove the energetic wavefield. The conventional F-K method is used to filter surface waves and converted refracted waves. The SVD method (Singular Value Decomposition) is then used to extract refracted waves. The different steps of the processing sequence are: amplitude recovery, deconvolution by spectrum equalization, wave separation by SVD and F-K filters, normal moveout (NMO) with constant velocity for quality control.

The shot point presented here is an end-on spread shot composed of 96 traces. The distance between 2 adjacent geophones was 1 m. The source was a weight dropper (see Figure 2.6-c in the "Refraction surveying" chapter). There was no data filtering at the acquisition, consequently the shot was highly corrupted by surface waves (pseudo Rayleigh modes). This shot type is often called a noise profile. It can be used for the analysis of surface waves and also to define the acquisition parameters for near-surface 3D acquisition.

Figures 4.7 to 4.8 show the step-by-step processing sequence of the noise profile. At each stage the data are shown both in the time-distance domain, and in the frequency-wavenumber domain (f-k domain).

Figure 4.7-a shows the raw shot. The seismic trace close to the source is saturated. We observed a very strong attenuation of seismic amplitudes with the offset. After amplitude compensation (Figure 4.7-b), the direct wave, refracted waves, air wave and surface waves were clearly visible. The f-k amplitude spectrum shows that most of the energy is limited in wave number up to 0.25 c/m. Consequently, a geophone interval of 2m allowed the data to be recorded without spatial aliasing. A deconvolution process was applied to the data to increase the vertical resolution by spectral balancing and to facilitate the wave separation (Figure 4-d). The wave separation process involves the extraction of a wave by an apparent velocity filter defined in the f-k domain and then the subtraction of the estimated wave from the dataset to obtain a residual section. The process is carried out iteratively for different waves or seismic events. Figure 4.7-d shows the estimation of the air wave and the Rayleigh wave.

The associated residual section is shown in Figure 4.8-a. On the 2D amplitude spectrum, we note that the energy is concentrated in the 0 to 0.2 c/m wave number interval. It is also possible to see that the air wave is aliased for frequencies larger than 200 Hz and appears with negative apparent velocities. The events with negative apparent velocities are shown in Figure 4.8-b, while the associated residual section (Figure 4.8-c) mainly contains the refracted events (Figure 4.8-d). The residual section associated with the refracted events shows events of very weak amplitude with high apparent velocities in the 60 to 150 ms time interval (Figure 4.9-a). These events are reflected events. On the same section, we can observe low apparent velocity events which are residues of direct waves and air waves (Figure 4.9-b). The residual section associated with the low apparent velocity events shows reflected events (Figure 4.9-c), which are flattened after NMO corrections (Figure 4.9-d).

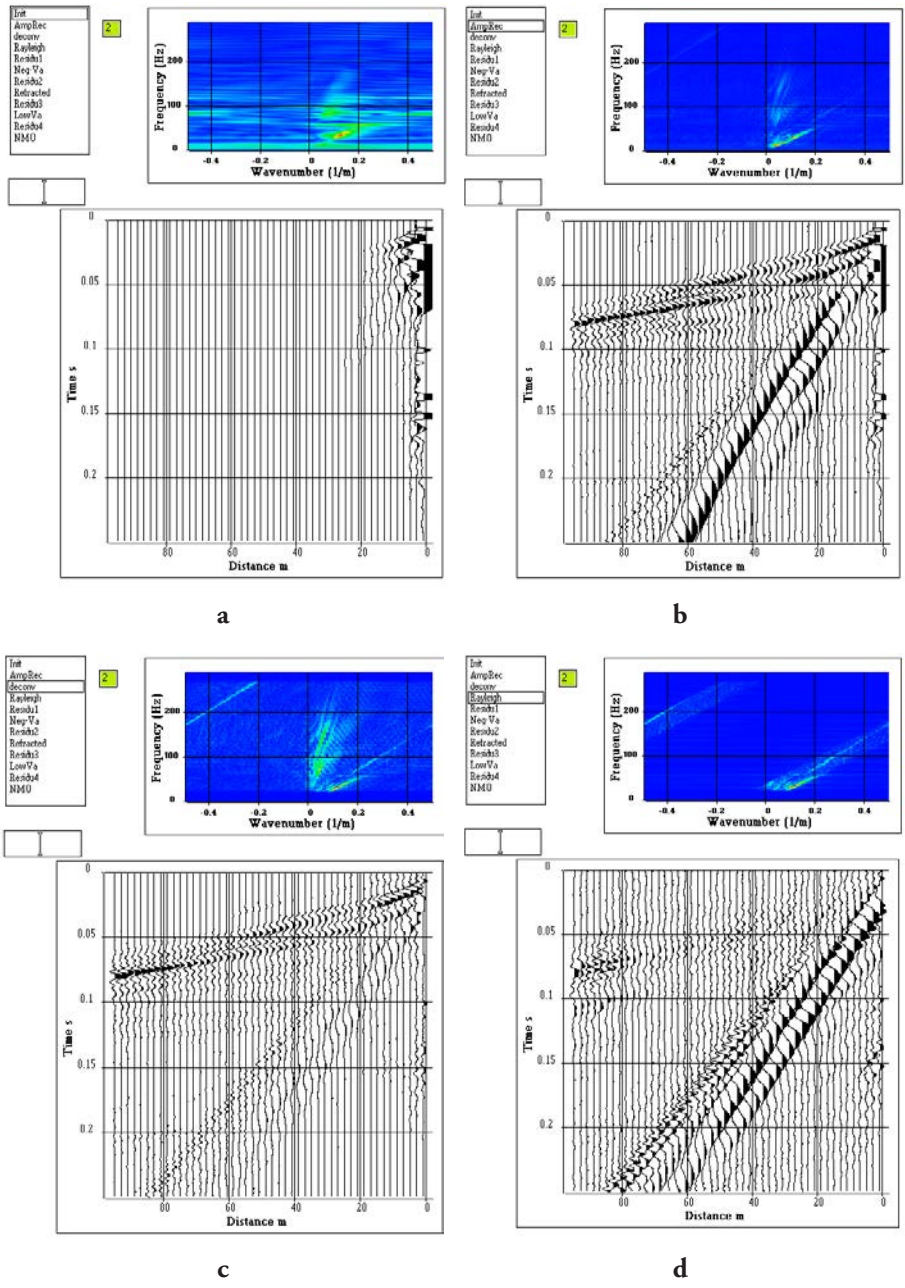

Figure 4.7 *Noise profile processing: (a) raw shot, (b) amplitude compensation, (c) deconvolution, (d) extraction of air wave and surface waves.*

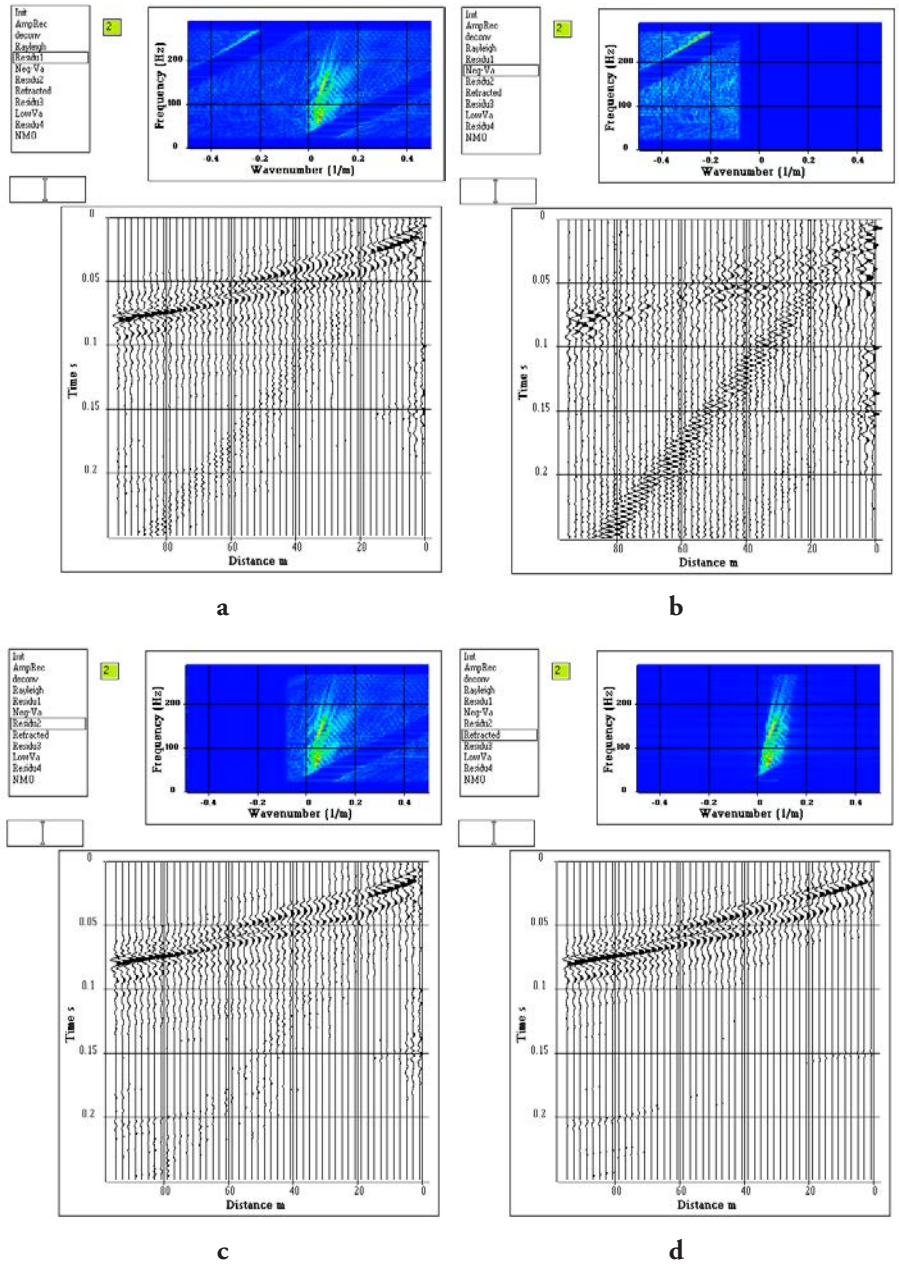

Figure 4.8 *Noise profile processing: (a) first residual section, (b) seismic events with negative apparent velocities, (c) second residual section, (d) direct and refracted waves.*

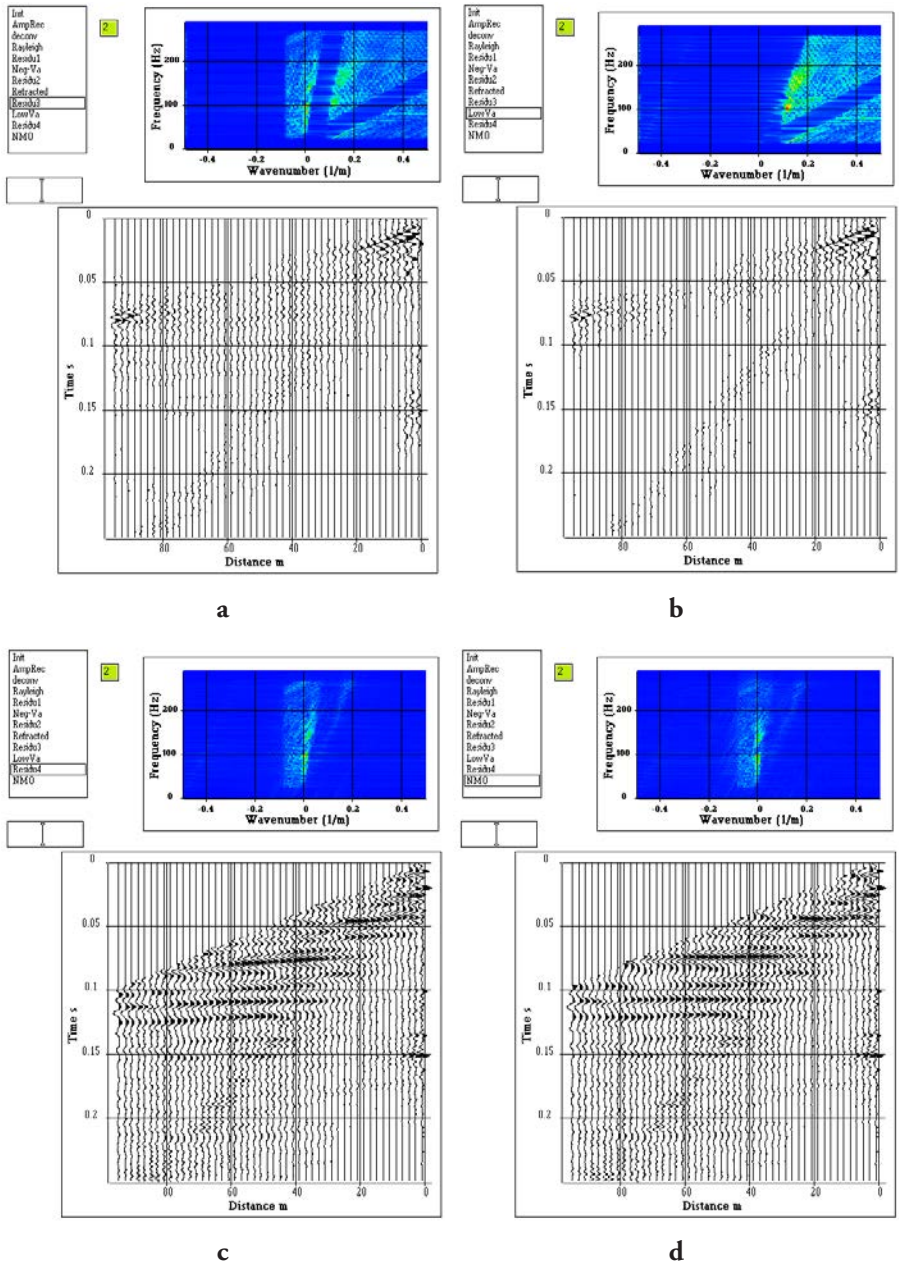

Figure 4.9 *Noise profile processing: (a) third residual section, (b) low apparent velocity events, (c) fourth residual section, (d) reflected waves after NMO corrections.*

The analysis of the noise profile shows that a seismic acquisition with a minimum offset of 40 m and a geophone interval of 2 m can be implemented to obtain reflected events in the 60 to 150 ms time interval. These parameters were checked in a 3D configuration, with an elementary cross-spread composed of 48 geophones (Figure 4.10-a). The distance between 2 adjacent geophones was 2 m. The source was a weight dropper situated in the middle of the recording, with a lateral offset of 45 m. Figures 4.10 to 4.12 illustrate the step-by-step processing sequence.

Step 1: Display of the shot point before and after band pass filtering (Figure 4.10-b). In the upper part, we can see the refracted wave, the high frequency air wave and the low frequency surface wave. In the lower part, after filtering the air waves and surface waves are attenuated.

Step 2: Display of the shot point after amplitude recovery and band pass filtering (Figure 4.10-c): refracted waves can be seen in the first arrivals, and a reflected wave can be hypothesized after 0.1s.

Step 3: Display of the shot point after amplitude recovery, band pass filtering and deconvolution (Figure 4.10-d). The deconvolution increases the vertical resolution and facilitates wave separation.

Step 4: Extraction of refracted waves by SVD filter (Figure 4.11-a).

Step 5: Calculation of the first residual section: in the F-K diagram one can see events with wave numbers close to 0, and frequencies ranging between 50 Hz up to 200 Hz (Figure 4.11-b). Events with low frequencies and wave numbers ranging between -0.1 and 0.1 c/m can also be seen.

Step 6: Extraction of seismic waves with low apparent velocities by F-K filter (Figure 4.11-c).

Step 7: Calculation of the second residual section (Figure 4.11-d): one can mainly see reflected waves.

Step 8: Reflected waves after static corrections (Figure 4.12-a)

Step 9: Time variant velocity model used for the NMO correction (Figure 4.12-b)

Step 10: NMO correction with time variant velocity model. The reflected waves are flattened (Figure 4.12-c). Seismic horizons between 0.04 and 0.12 s can be seen.

Step 11: Time to depth conversion of the seismic section (Figure 4.12-d). The upper part of the figure shows the depth versus time law. On the seismic section, a continuous layer can be seen above 60 m. The layers below 60 m are situated in the bedrock.

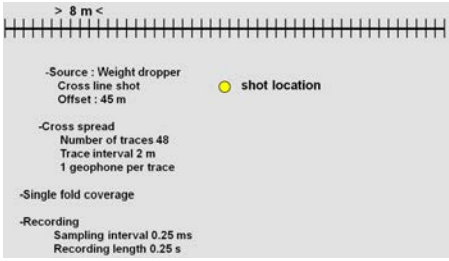

a

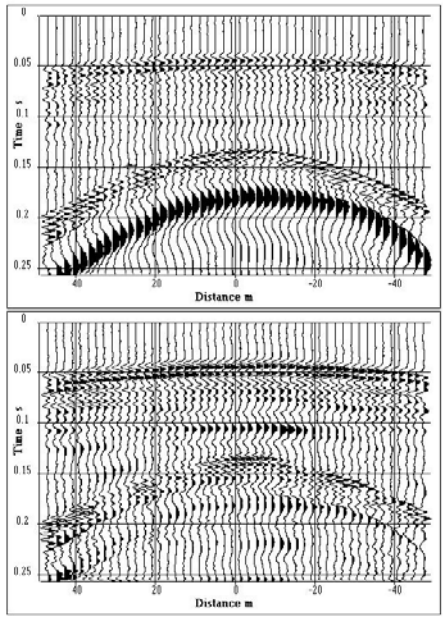

b

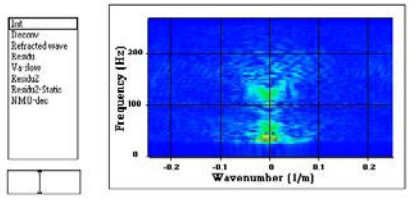

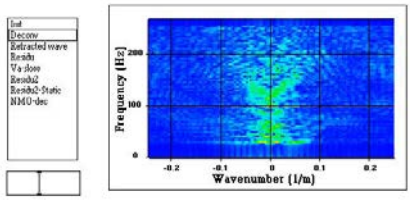

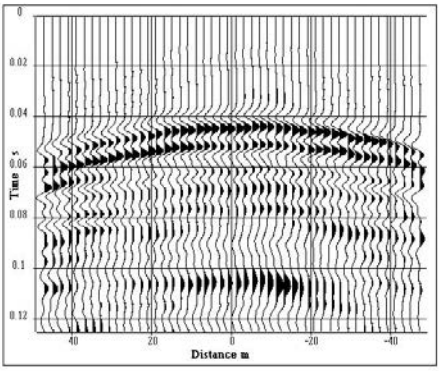

c

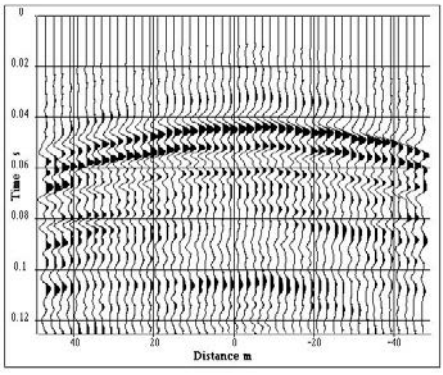

d

Figure 4.10 *Elementary cross-spread shot: (a) acquisition spread, (b) raw shot before and after filtering, (c) amplitude compensation, (d) deconvolution.*

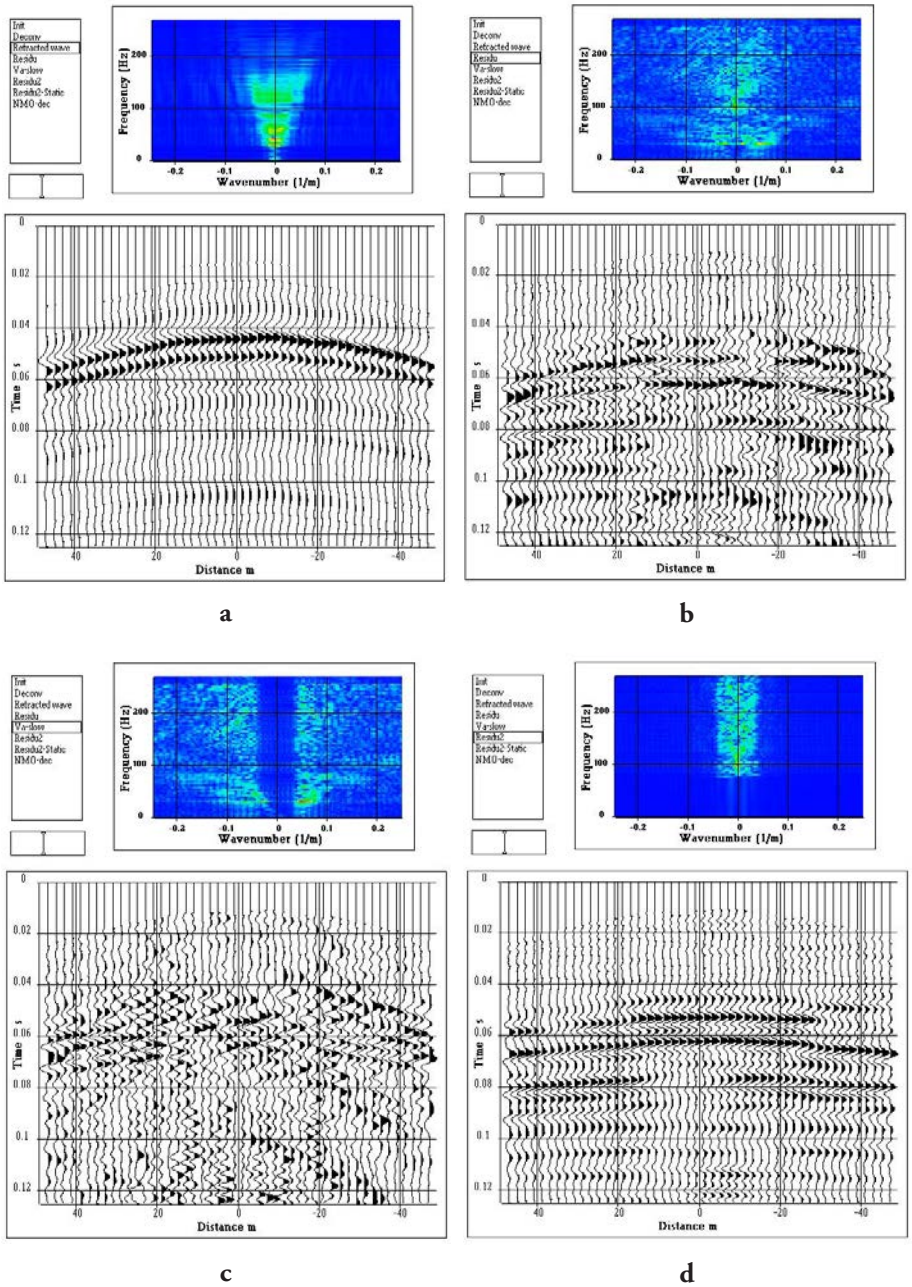

Figure 4.11 *Elementary cross-spread shot: (a) refracted wave, (b) first residual section, (c) low apparent velocity events, (d) Second residual section.*

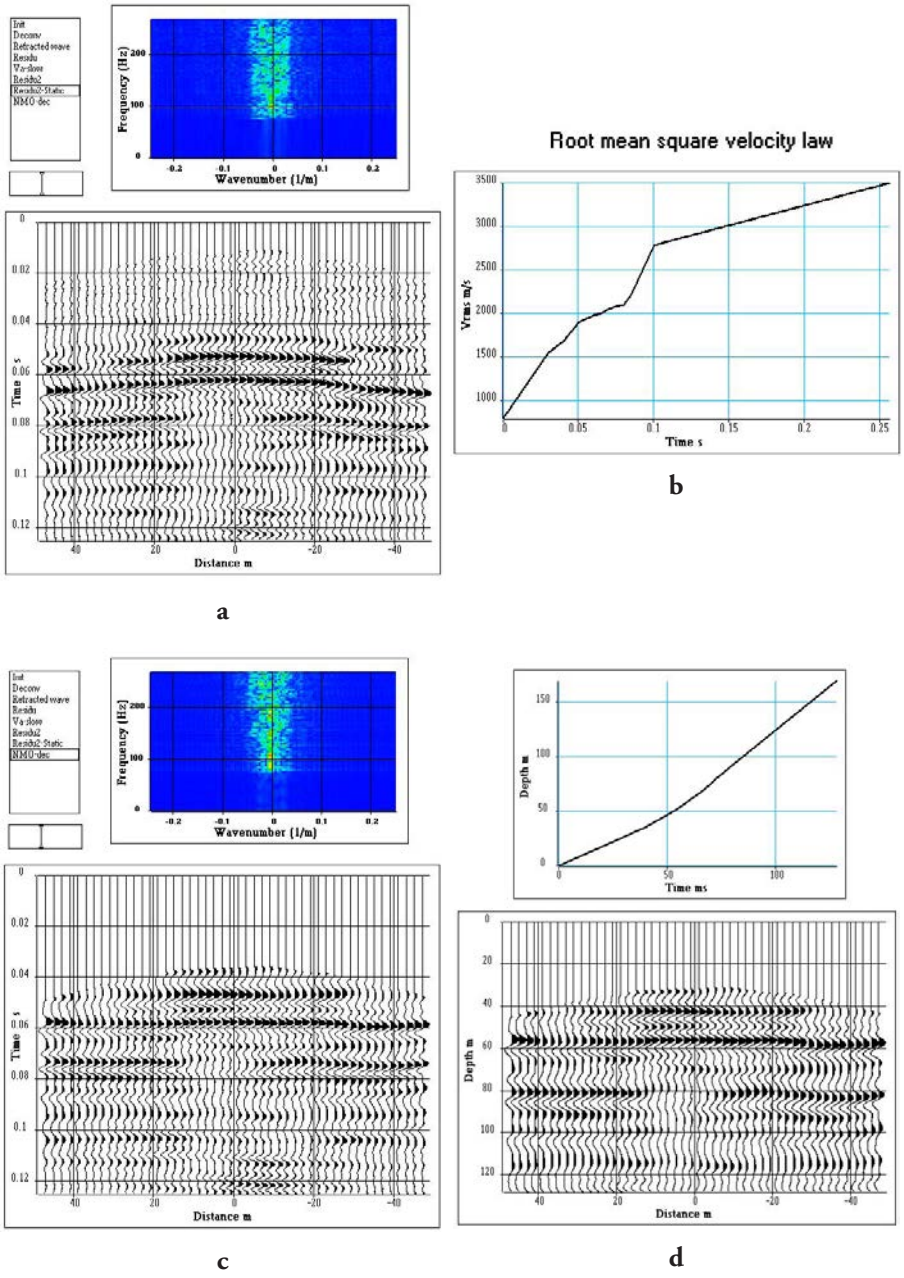

Figure 4.12 *Elementary cross-spread shot: (a) second residual section after static corrections, (b) Rms velocity model, (c) section after NMO correction, (d) section in depth.*

The results obtained by the analysis of the noise profile and the elementary cross-spread enabled the acquisition parameters for a 3D survey and processing flow to be defined, to obtain a significant 3D cube in multiple fold (up to 22).

The seismic spread was composed of a receiver spread and a source spread. The receiver spread, shown in green, had 2 receiver lines. The receiver line direction is known as the in-line direction. The distance between the receiver lines was 4 m. There were 24 geophones per line. The distance between the geophones was 2 m.

The source spread, shown in yellow, was composed of 11 source lines oriented perpendicular to the receiver lines. 11 shots were fired per line. The distance between the shots was 2 m. The distance between the source lines was 4 m. The source lines and the receiver lines were perpendicular.

The distance between the receiver spread and the source spread was 4 m. There was no overlap between the source and the receiver spread.

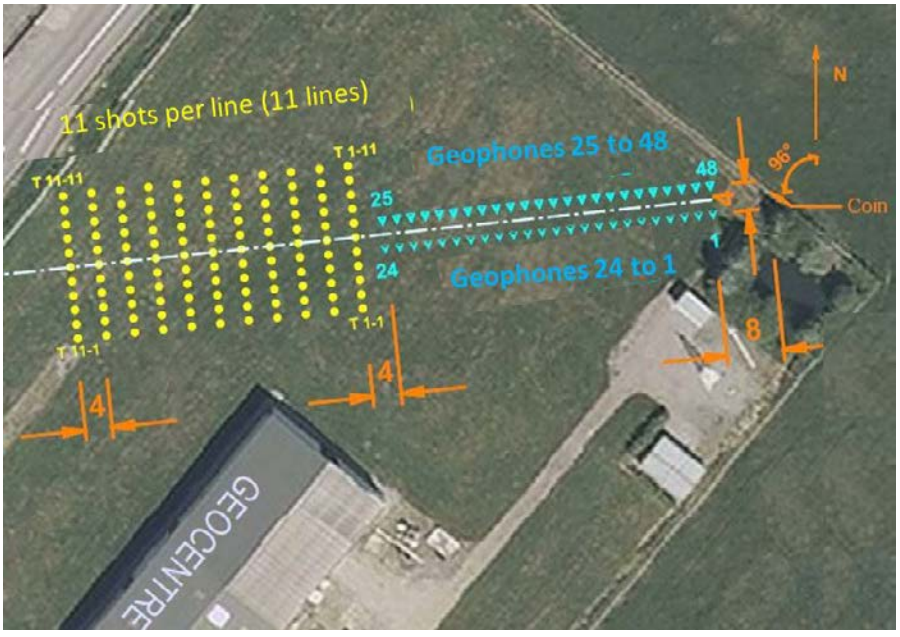

Figure 4.13 *3D Seismic spread.*

Due to the geometry of acquisition, the geometric fold was symmetric. Figure 4.14 shows the fold variation, which varied from 0 to 22.

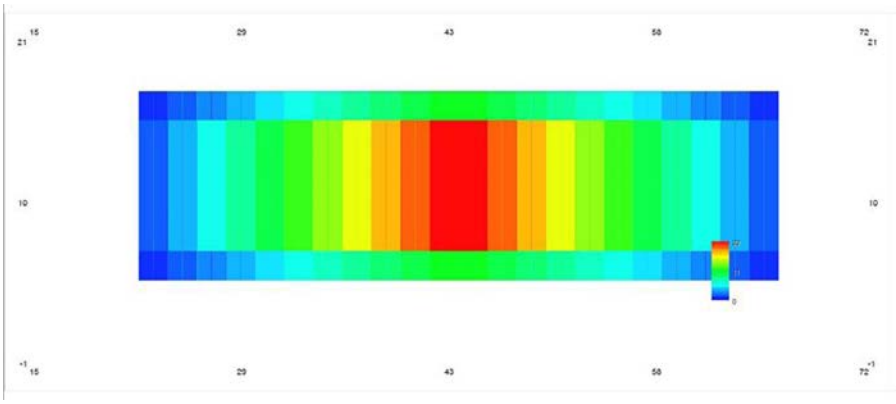

Figure 4.14 *Fold variation. Variation was from 0 to 22. The horizontal axis in the figure is the in-line direction. The vertical axis is the cross-line direction.*

The processing was carried out with the SPW software developed by Parallel Geoscience (Mari and Herold, 2015). The listening time was limited to 250 ms, the sampling time interval was 0.5 ms. Figure 4.15 shows a shot point example.

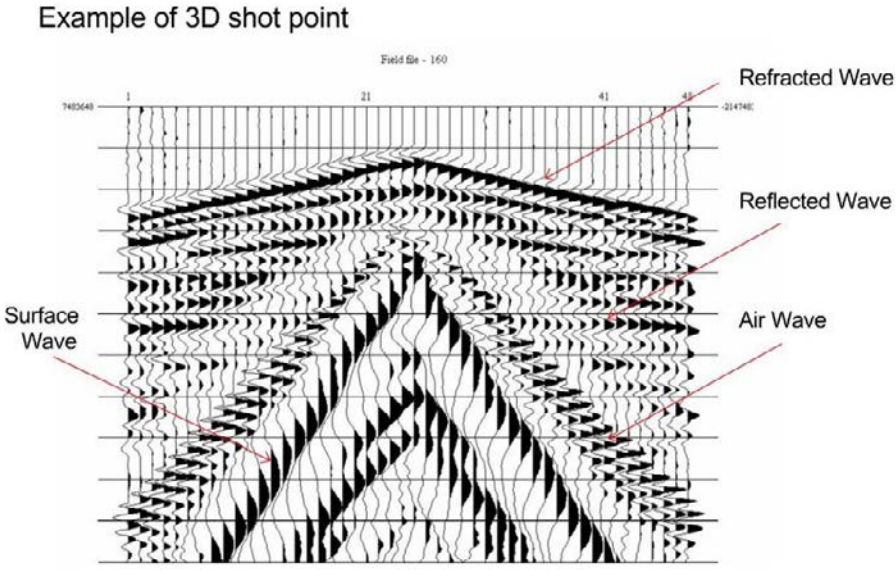

Figure 4.15 *Example of a 3D shot point. It is possible to identify the refracted wave, reflected wave, air wave and surface wave. The air wave is aliased.*

The processing sequence of each shot includes: amplitude recovery, deconvolution in the 15-150 Hz frequency bandwidth, tail mute, and static corrections (Figure 4.16). The deconvolution was carried out to increase the resolution and attenuate the surface waves. A tail mute was used to eliminate air waves and surface waves. The static corrections were performed to compensate the effects of the weathering zone. In the example, the 3D static corrections are very weak.

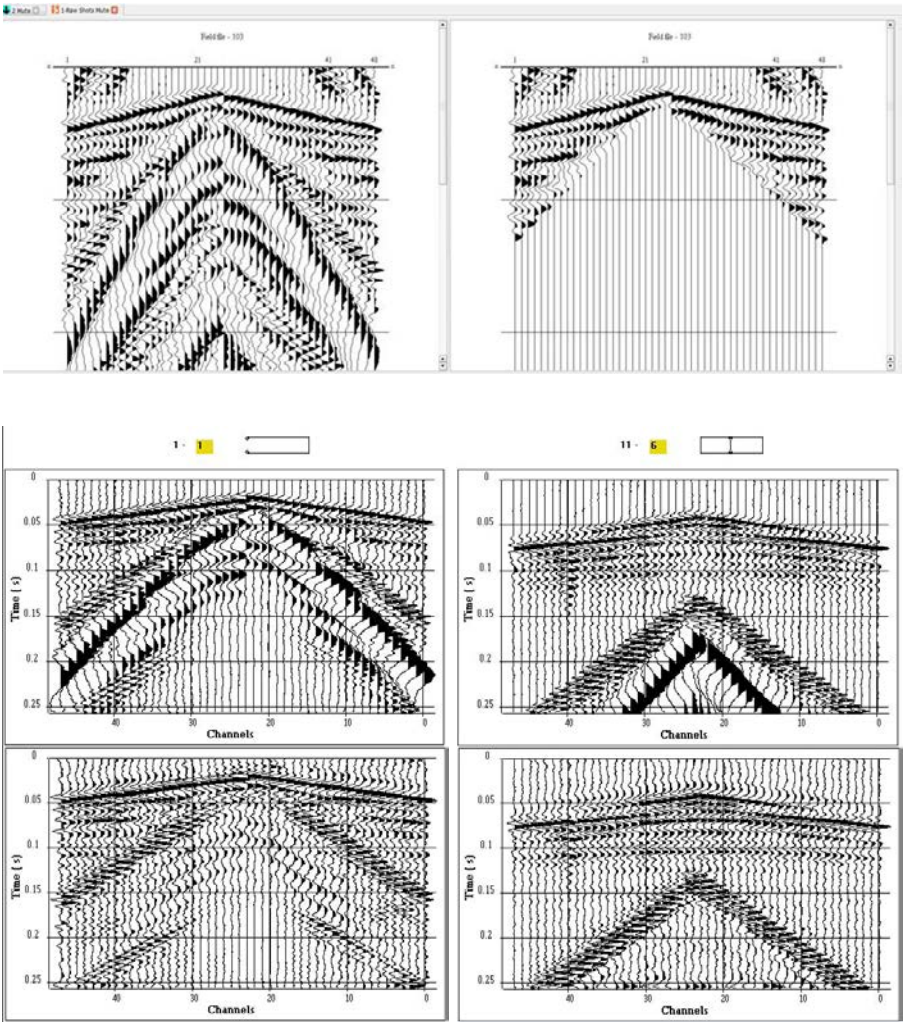

Figure 4.16 *Some processing steps. Top: example of a raw shot before and after tail mute; bottom: example of 3D shot point before and after deconvolution; left: near offset 3D shot point. The shot point is shot number 1 on line 1; right: far offset 3D shot point. The shot point is shot number 6 on line 11. A reflected event is clearly visible at 100 ms, after deconvolution.*

The data were sorted in common midpoint (CMP) gathers. NMO corrections were carried out with a stacking velocity model obtained by velocity analysis. Surface consistent residual statics were calculated to enhance the signal to noise ratio and preserve the high resolution of the data in the CMP stack procedure.

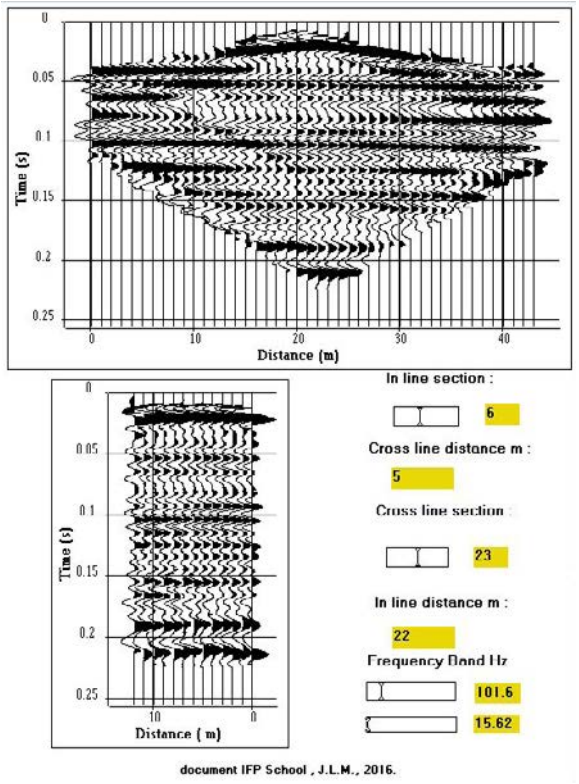

Figure 4.17 *CMP stacked sections. The high-resolution 3D cube revealed near-surface seismic horizons between 50 and 200 ms.*

The 3D block is composed of 13 in-line sections 1 m apart. Each section is composed of 44 CMP points 1 m apart. Figure 4.17 shows an example of in-line and cross-line seismic sections extracted from the 3D block. The two sections presented (section 6 in the in-line direction, and section 23 in the cross-line direction) intersect in the middle of the 3D block. They have been filtered in the 15-150 Hz bandwidth, which provides an excellent signal-to-noise ratio. The CMP point located at the intersection of the in-line seismic section No. 3 and cross-line No. 6 is located about twenty meters from a borehole in which a vertical seismic profile (VSP) was recorded. The VSP (Figure 4.18, top) was used to obtain an interval velocity model and a time versus depth law, which was used to perform the time to depth conversion of the 3D block (Figure 4.18, bottom).

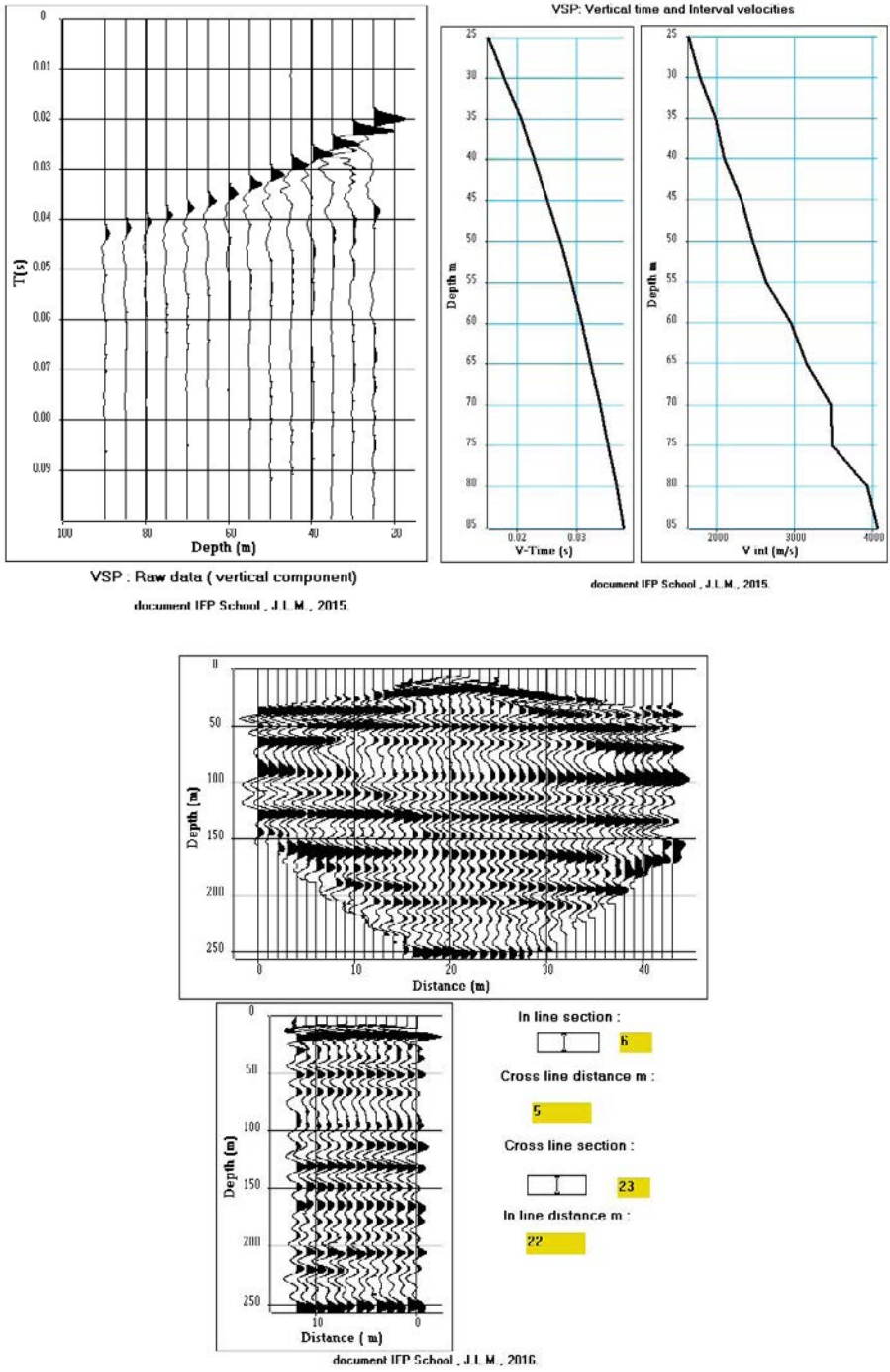

Figure 4.18 *VSP and 3D block in depth. Top: Raw VSP and VSP logs (vertical time and interval velocities); bottom: 3D block in depth.*

4.4 A Hydrogeology example

This example concerns the imaging of a near-surface karstic reservoir at the Hydrogeological Experimental Site of Poitiers. The field case has already been discussed in the "Refraction surveying" chapter.

Preliminary studies led to the selection of the following spreads for 3D imaging. The detonating impulse source was selected to record high frequency data and to reduce the air wave effect. To preserve the high frequency content of the data and to have an accurate picking of the refracted wave, a single geophone per trace was used.

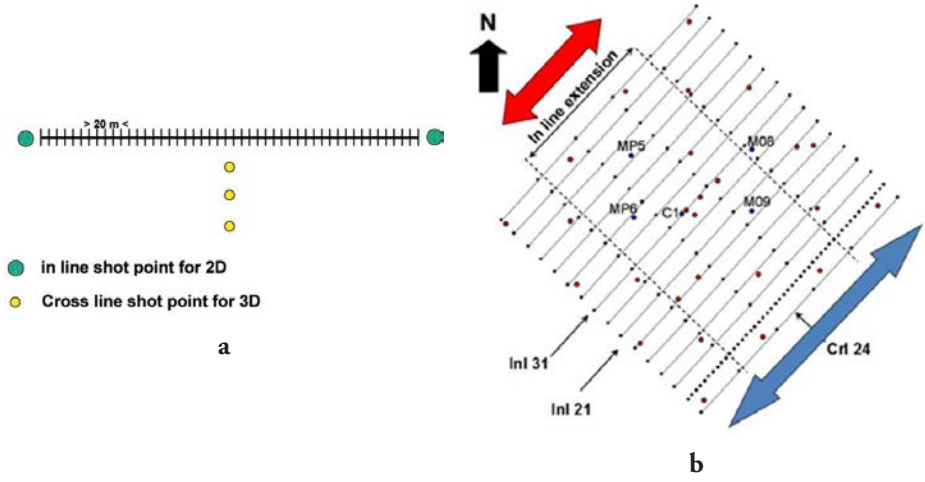

Figure 4.19 *Seismic spreads and field implementation of seismic lines. (a) Seismic spreads - A direct shot and reverse shot are fired in line to obtain 2D seismic images. Several cross-line shots are fired to obtain 3D seismic images. (b) Seismic line implementation: the distance between 2 adjacent lines is 15 m. Red points indicate well locations.*

To avoid spatial aliasing, a 5 m distance between two adjacent geophones was selected. Due to the dimensions of the area, it was not possible to extend the length of the seismic line over 250 m in the in-line direction. Consequently, a 48-channel recorder was used. In the cross-line direction, the extension of the area did not exceed 300 m. As a result, 21 receiver lines were implemented, with a 15 m distance between adjacent lines. For the refraction survey, a direct shot and a reverse shot were recorded per receiver line. For the reflection survey, 3 shot points in the cross-line direction were fired per receiver line. The range of offsets was selected to optimize the quality of the seismic image in the reservoir zone, between 40 and 130 m. The minimum offset distance was chosen as 40 m to reduce the

influence of surface waves. The distance between 2 adjacent shot points in the cross-line direction was chosen to be 10 m. Figure 4.19 shows the selected seismic spreads and the map locating the seismic lines. The red points indicate the location of the wells.

The processing sequence has been described in detail in several publications (Mari and Porel, 2007; and Mari and Delay, 2011), so it is only briefly explained here. Each shot point was processed independently (both in the cross-line direction and in the in-line direction) to obtain a single-fold section with a sampling interval of 2.5 m (half the distance between 2 adjacent geophones) in the in-line direction. The processing of an in-line direct and reverse shot gather enabled a single-fold section with an in-line extension of 240 m to be obtained (indicated by a blue arrow on the seismic line map, Figure 4.19-b) while a cross-line shot gather has provided a single-fold section with an in-line extension of 120 m (indicated by a red arrow on the seismic lines map, Figure 4.19-b).

A 3D seismic refraction tomography (Mari and Mendes, 2012, see also the "Refraction Surveying" chapter) was carried out to map the irregular shape of the top of the karstic reservoir, and to obtain static corrections and a velocity model of the overburden. To add information to the inversion procedure, we used in-line and cross-line cross shots simultaneously, with an offset of 60 m. The shots were selected to ensure that the refracted wave was the first arrival wave, regardless of the source-receiver distance. The picked times of the first seismic arrivals for all shots (in-line and cross-lines shots), the depth map of the top of the reservoir (defined from the wells), and the velocity model obtained by the Plus–Minus method were used as input data for the inversion procedure (see "Refraction surveying" chapter). The inversion results obtained with 3D data emphasize the previously mentioned geological structures, providing a better understanding of their alignments and shape (corridor of fractures). Furthermore, no cavities were detected near the surface.

The processing sequence includes: amplitude recovery, deconvolution, wave separation (SVD method for extracting refracted waves and combining the SVD and F-K methods for filtering surface waves), static corrections (obtained by inversion tomography) and NMO corrections. A VSP was recorded in well C1. VSP data were processed to obtain a time versus depth relationship and a velocity model. The velocity model was used to apply the NMO corrections. The VSP time versus depth law was also used to convert the time sections into depth sections with a 0.5 m depth sampling interval.

For illustration, the elementary cross-spread corresponding to geophone line 11 with a 60 m lateral source offset is shown in Figure 4.20.

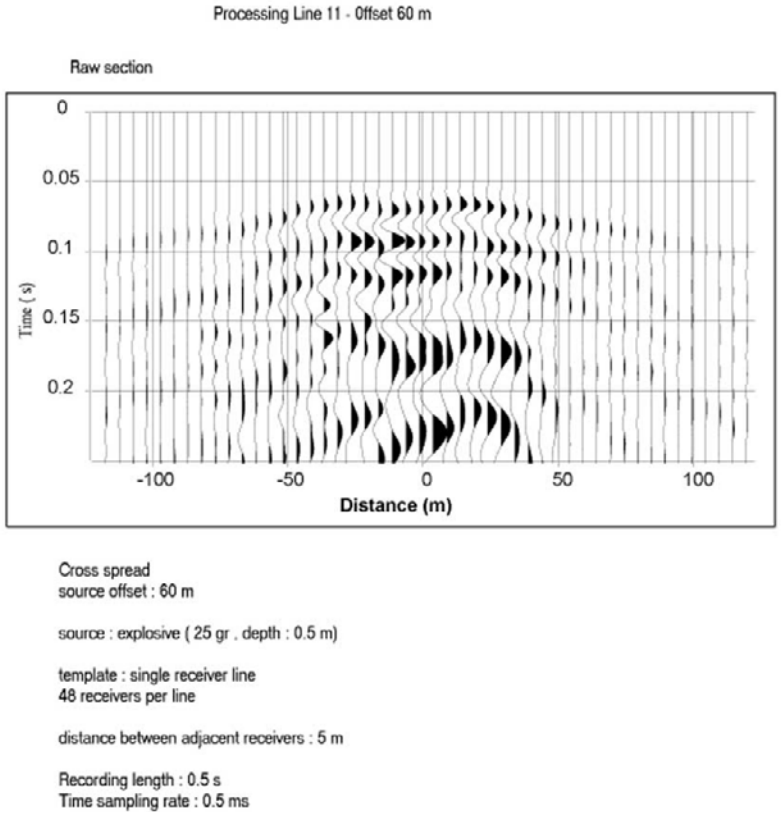

Figure 4.20 *Example of an elementary cross-spread.*

Figures 4.21 and 4.22 show the first steps of the processing of the cross spread recorded on line 11 with a 60 m source offset. After amplitude recovery (Figure 4.21, top left) and deconvolution (Figure 4.21, bottom left), the wave separation procedure is applied as follows:

- Extraction of the refracted wave by SVD filter (Figure 4.21, top right).
- Subtraction of the refracted wave from the initial section to obtain the first residual section (Figure 4.21, bottom right). The residual section shows mainly surface waves with low apparent velocities.
- Extraction of the low apparent velocity events by F-K filter (Figure 4.22, top left).
- Subtraction of the low apparent velocity events from the first residual section to obtain the second residual section (Figure 4.22, bottom left).

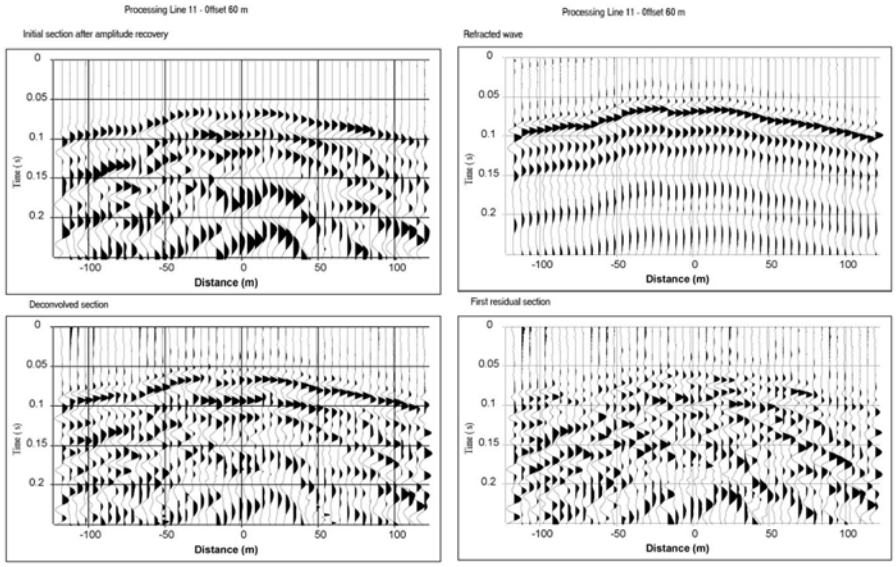

Figure 4.21 *Processing of geophone line 11 with a 60 m source offset; top left: amplitude recovery, bottom left: deconvolution, top right: refracted wave, bottom right: first residual section.*

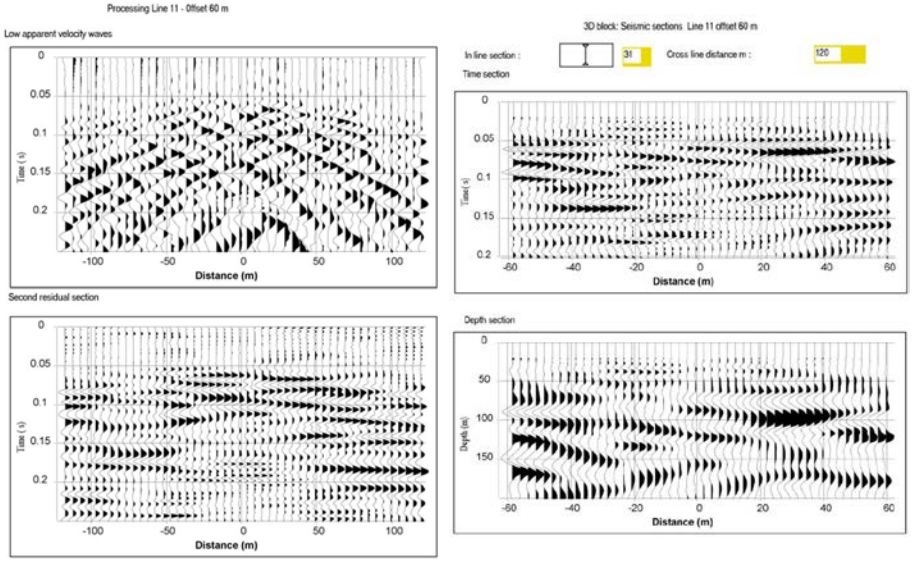

Figure 4.22 *Processing of geophone line 11 with a 60 m source offset; top left: low apparent velocity waves, bottom left: second residual section, top right: time section, bottom right: depth section.*

The second residual section shows high apparent velocity seismic events with a poor lateral continuity. This could be reflected or diffracted waves corrupted by residual noise. The velocity model was used to apply the NMO correction to the residual section to obtain a zero-offset section at normal incidence.

The same processing sequence was applied to the 60 individual shot points to obtain 60 zero offset sections. The 60 sections were merged to create the 3D block. The width of the block in the in-line direction is 120 m. The abscissa zero indicates the location of the source line. The abscissa of the reflecting points varies between –60 m and +60 m in the in-line direction; the distance between two reflecting points is 2.5 m. Due to the geometry of acquisition, the shot point recorded on geophone line 11 with a 60 m source offset becomes the in-line section 31 (Figure 4.22, top right). The VSP time versus depth law measured at well C1 was used to convert the time sections into depth sections with a 0.5 depth sampling interval. The depth conversion of time section 31 is presented in Figure 4.22 (bottom right). In the 30 to 120 m depth interval, it can be noted that the vertical seismic resolution is insufficient to describe the heterogeneities inside the reservoir. The only way to increase the vertical resolution is to apply a deconvolution of the wave number to the depth sections. The result for depth section 31 is presented in Figure 4.23-a (upper part). A significant improvement of the vertical resolution is thus obtained.

After deconvolution, it was assumed that the seismic trace represents the reflectivity function of the geological model. Integration with respect to depth enabled the deconvolved seismic trace to be constrained to obtain an estimate of the interval velocity function versus depth. For this purpose, after deconvolution and integration, a Wiener filter (Mari *et al.*, 2015) was applied to the seismic traces to convert the amplitude sections into velocity. The Wiener filter is designed to obtain an optimum fit between the acoustic velocity log at well C1 and the associated deconvolved and integrated seismic trace (Figure 4.23-b). The Wiener operator thus obtained was applied to all the deconvolved and integrated traces of the 3D block to transform an amplitude block into a 3D pseudo velocity block in depth. The result obtained with the in-line depth section 31 is shown in Figure 4.23-a (bottom). The procedure was validated by measuring correlation coefficients between estimated seismic pseudo velocity logs and acoustic logs at wells MP6, MP5, M8 and M9 (Figure 4.19-b).

The 2D direct and reverse shots were processed in the same way to laterally extend the 3D block. All pseudo-velocity depth sections were merged to create the 3D block. The width of the block in the in-line direction is 240 m, and 300 m in the cross-line direction.

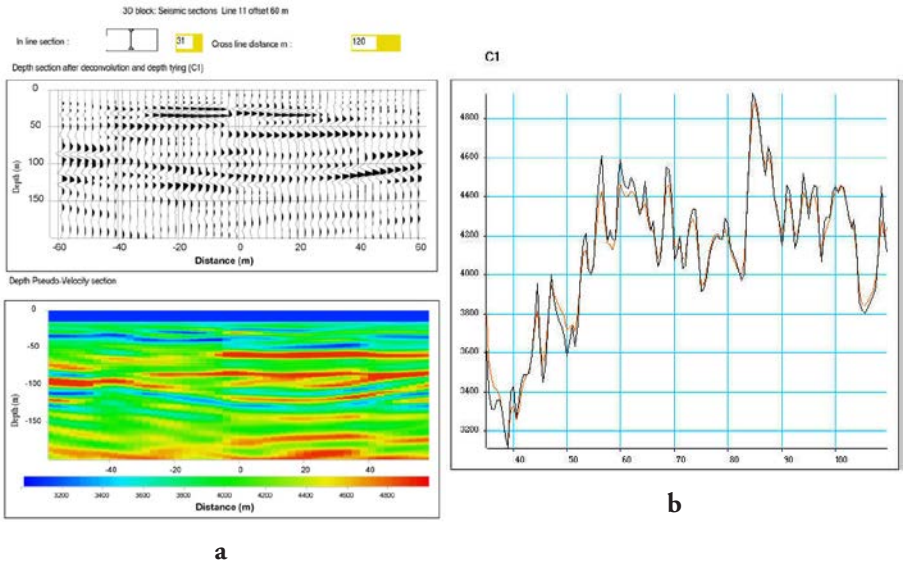

Figure 4.23 *Example of deconvolved and pseudo velocity depth sections (in-line section 31). (a) Depth section after deconvolution and depth tying (top). Depth pseudo velocity section (bottom). (b) Velocity functions at well C1: velocity function derived from acoustic measurement (black curve), velocity function derived from seismic trace (red curve).*

In the in-line direction, the abscissa zero indicates the location of the source line. The abscissa of the reflecting points varies between –120 m and 120 m in the in-line direction. The distance between two reflecting points is 2.5 m. In the cross-line direction, the distance between two reflecting points is 5 m.

The pseudo velocity sections of the 3D block thus obtained were merged with those obtained by refraction tomography (see "Refraction surveying" chapter) to create a 3D extended velocity model from the surface (Figure 4.24). Figure 4.24 (top left) shows the results obtained for the in-line 31 seismic section extracted from the 3D extended velocity model. It also shows the velocity map at a depth of 87 m (Figure 4.24, top right). The 3D velocity model shows the large heterogeneity of the aquifer reservoir in the horizontal and vertical planes. To quantify the porosity variations within this aquifer, the seismic interval velocities were first converted into resistivity values. For this purpose, the empirical relationship between seismic velocity and resistivity proposed by Faust (1953) was used. Resistivity values were then converted into porosity values, using Archie's law (1942). Figure 4.24 (bottom) shows the pseudo velocity and porosity seismic sections for the in-line 21 and cross-line 24.

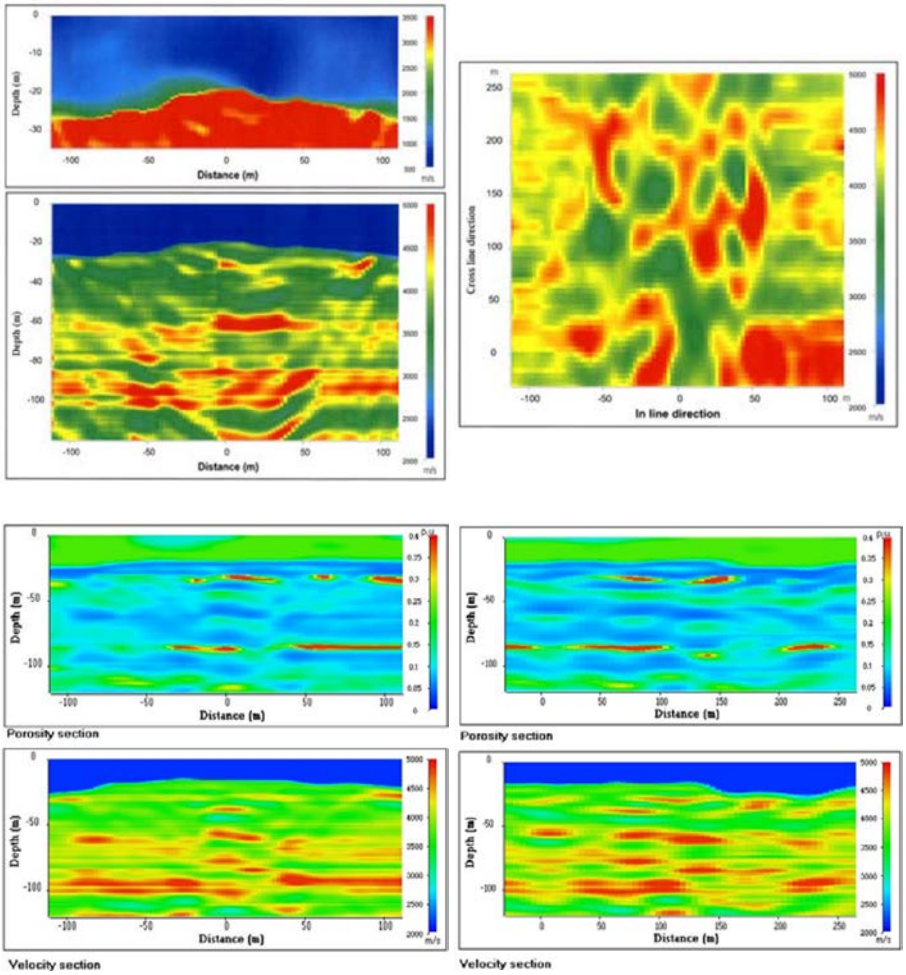

Figure 4.24 *3D seismic processing. Top left: in-line 31 pseudo-velocity section (upper part: close up of 0 to 35 m depth interval). Top right: pseudo-velocity map at 87 m depth. Bottom left: in-line 21 pseudo-velocity and porosity seismic sections. Bottom right: cross-line 24 pseudo-velocity and porosity seismic sections.*

The resulting 3D seismic pseudo-porosity block revealed three high-porosity layers, at depths of 35 to 40 m, 85 to 87 m and 110 to 115 m. The 85 to 87 m layer is the most porous, with porosities higher than 30 %, which represents the karstic part of the reservoir. Figure 4.25 shows the distributions of porous bodies in the 80 to 90 m and 100 to 120 m depth intervals.

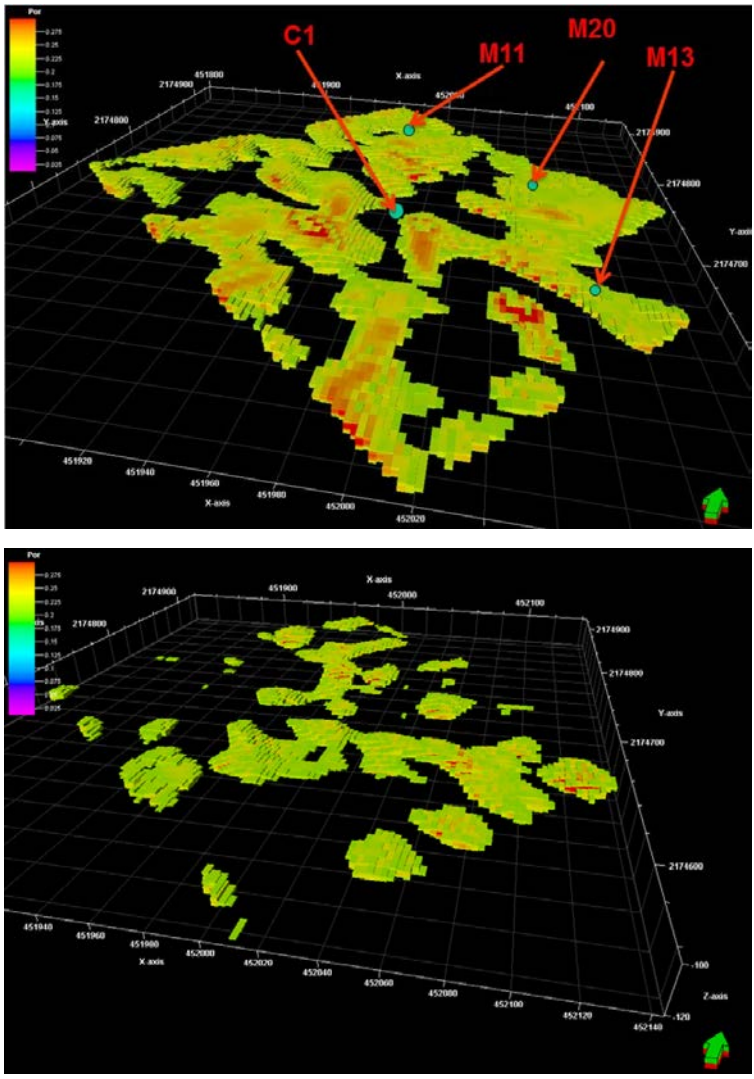

Figure 4.25 *Distribution of karstic bodies. Top: the 80 to 90 m depth interval. Bottom: the 100 to 120 m depth interval.*

The 3D block is composed of elementary cells (2.5 m in the in-line direction, 5 m in the cross-line direction, and 1 m deep), which clearly show the connectivity of the karstic bodies. The local validation of the results obtained by the 3D seismic method was achieved using full waveform acoustic data and VSP, recorded in 11 wells in 2014 and 2015 respectively (Mari and Porel, 2018).

4.5 Conclusion

Seismic reflection technology has been developed for the oil industry. The 3D seismic spread designs require the use of telemetric recording systems. Processing sequences enable high-resolution 3D seismic blocks to be obtained, due to sophisticated algorithms (3D prestack depth migration, full waveform inversion…) that are implemented on high performance computers.

In this chapter we have shown that it is possible to obtain very high-resolution 3D blocks for near surface applications with very basic seismic spreads (48 channels recorders, a single geophone per trace, light seismic source). Near surface studies require specific test phases to define the optimum acquisition parameters (minimum offset, geophone interval). The processing sequence must be carefully adjusted to the field data, especially for the wave separation.

In the near-surface karstic reservoir imaging example (Hydrogeological Experimental Site of Poitiers), we have shown that the velocity distribution obtained by refraction tomography in the first 30m can be merged with the velocities extracted from the amplitude of the reflected events, to obtain a continuous velocity model from the surface up to a depth of 120 m.

The spread, designed for near-surface reflection surveying, can be used for refraction surveying and surface wave analysis. The results obtained using the different methods can be productively combined, which is explored further in the "Hybrid seismic methods" chapter.

References

Anstey N., 1986, Part 1: Whatever happened to ground roll? *The Leading Edge*, 5, 40-45, DOI:10.1190/1.1439239.

Archie G.E., 1942, The electrical resistivity log as an aid in determining some reservoir characteristics, *Petroleum Technology*, 146, 54-62.

Chaouch A., Mari J.L., 2006, 3D land seismic surveys: Definition of Geophysical parameters, Oil & Gas Science and Technology, *Rev. IFP.,* 61 (5), 611-630, DOI: 10.2516/ogst:2006002.

Cordsen A., Galbraith M., Peirce J., 2000, Planning land 3D seismic surveys – SEG Series No. 9, Bob A. Hardage Ed.

Faust, L.Y., 1953, A velocity function including lithologic variation, *Geophysics*, 18, 271-288.

Galbraith M., 2000, 3D seismic survey design: a solution, *First break*, 18 (5), 171-176.

Lansley M., 2000, 3D seismic survey design: a solution, *First break*, 18 (5), 162-166.

Mari J.L., Glangeaud F., Coppens F., 1997, *Signal processing for geologists and geophysicists*, Technip Ed., Paris, ISBN: 2-7108-0752-1

Mari J.L., Porel, G., 2007, 3D seismic imaging of a near-surface heterogeneous aquifer: a case study, *Oil and Gas Science and Technology, Rev IFP* 63, 179-201. DOI: 10.2516/ogst/2007077.

Mari J.L., Delay F., 2011, "Contribution of Seismic and acoustic methods to reservoir model building", in *Hydraulic Conductivity / Book 1*, InTech-Open Access Publisher, ISBN 978-953-307-288-3, DOI: 10.5772/22051.

Mari J.L., Mendes M., 2012, High resolution near surface imaging of fracture corridors and cavities by combining Plus-Minus method and refraction tomography, *Near Surface Geophysics*, 10, 185-195, DOI: 10.3997/1873-0604.201 1052.

Mari J.L., 2015, Signal processing for geologists & geophysicists, e-book, DOI:10.2516/ifpen/2011002. http://books.ifpenergiesnouvelles.fr/ebooks/signal-processing/

Mari J.L., Porel G., 2018, Contribution of seismic and acoustic methods to the characterization of karstic formation, in Mari J.L., Vergniault C., 2018, *Well seismic surveying and acoustic logging*, EDP Sciences, ISBN (e-book): 7598-2263-8, DOI: 10.10051/978-2-7598-2263-8, https://www.edp-open.org/well-seismic-surveying-and-acoustic-logging

Mayne W.H., 1962, Common reflection point horizontal data stacking techniques, *Geophysics*, 27, 927-938, doi: 10.1190/1.1439118

Meunier J., 1998, Land 3D acquisition geometry: what is the cost of ground roll?, 68th annual international meeting, SEG, expanded abstracts, 58-61.

Meunier J., 1999, 3D geometry, velocity filtering and scattered noise, 69th annual international meeting, SEG, expanded abstracts, 1216-1219.

Meunier J., Gillot E., 2000, 3D seismic survey design: a solution, *First break*, 18 (5), 176-179.

Meunier J., 2011, Seismic acquisition from Yesterday to Tomorrow, distinguished instructor series, N° 14, SEG, ISBN 978-1-56080-281-5 (volume), ISBN 978-1-56080-086-06 (series)

Monk D., Yates M., 2000, 3D seismic survey design: a solution, *First break*, 18 (5), 180-183.

Musser J.A., 2000, 3D seismic survey design: a solution, *First break*, 18 (5), 166-171.

Robein E., 2003, *Velocities, Time-imaging and depth imaging, in Reflection seismics, Principles and methods*, EAGE Publications bv, ISBN 90-73781-28-0.

Vermeer G.J.O., Hornman K., 2000, Introduction to a 3D design problem, *First break*, 18 (5), 184-185.

Yilmaz O., 1987, Seismic data processing, SEG, Tulsa.